ISSN (e): 2250 – 3005 || Volume, 05 || Issue, 07 || July – 2015 ||
International Journal of Computational Engineering Research (IJCER)

Convection interaction in GaAs/LEC growth model

Reza Faiez[1], Farzad Najafi[2], Yazdan Rezaei[1]
[1] Solid State Lasers Research Group, School of Laser and Optics, Tehran, P.O.Box 11365-8486, Iran
[2] Research Institute of Petroleum Industry (RIPI), Tehran, P.O.Box 14665-137, Iran

ABSTRACT:
Fluid flow and heat transport are investigated for the GaAs melt rotating with its cylindrical container in a liquid encapsulated Czochraslki (LEC) growth system in which the flow pattern and temperature distribution in the melt are influenced by coupling of rotationally–driven forces to the thermal convection. The experimentally observed particular shape of the crystallization front was predicted numerically. The convective flow in the melt was studied by focusing on the Rayleigh-Benard and the baroclinic instabilities. Increasing the crucible rotation rate, the dominant convective cell found to pivot by a small angle in the meridional plane around the vorticity vector. This pivoting angle is directly related to the Ekman shear angle.

Keywords: *Computer simulation, Convection, Flow pattern, Coriolis forces, Interfaces, LEC growth*

I. INTRODUCTION

Low Prandtl-number ( ) semiconductor melt in a modified Czochralski (Cz) puller [1, 2] can be modeled as a two-dimensional Boussinesq fluid which rotates uniformly with its container. In the absence of an applied electromagnetic field, hydrodynamic processes relevant to crystal growth are classified into the following main groups: natural gravitational type convection, forced convection and the surface-tension driven convection. Typically, hydrodynamics and the associate transport phenomena in the system are quite complex because of their highly nonlinear and strong coupled interactions [3, 4]. The crystal quality is closely related to the crystallization front shape which depends on the heat balance at the vicinity of the front. Associated with a curved (convex or concave to melt) phase interface, the radial non-uniformity of the thermal history affects the crystal structure due to the formation of facets on the oxides growth interface [5]. In the case of semiconductors such as GaAs and InP, the density of the dislocations is a direct consequence of thermal stress in the crystal during the process. The maximum stresses which occur at the crystal periphery were found [6, 7] to be related to the growth interface morphology. The gull-winged shape GaAs phase boundary, revealed by different model calculations [8, 9], is well supported by experimental data [10, 11]. This typical interface shape, concave to melt ( ) at periphery and convex ( ) to melt in the center, strongly depends on the flow field structure [12]. Therefore, the interface destabilization, leading to thermal stresses and high dislocation density in the crystal, is mainly due to the convective instabilities in the melt.

Hydrodynamic stability, concerning the stability and instability of the fluid motions, has been largely studied in the last decades [13, 14]. Experimental data on the regime diagram of different fluids, each contained in a rotating cylindrical annulus and subjected to an imposed radial temperature gradient, were reported first by Fein and Pfeffer [15]. Their results were summarized in the form of two-parameter diagrams (thermal Rossby number vs. Taylor number) for different Pr numbers. For moderate and low Pr-number fluids, namely water ( ) and mercury ( ), they have displayed the well-known knee type (or the anvil shape) diagrams which characterize the transition from axisymmetric flow to regular baroclinic waves. The anvil-shape regime diagram for moderate Pr-number fluid, apart from the baroclinic regular wave, revealed the upper and the lower symmetric regimes. While the flow in the lower one is established by diffuse effects, the axisymmetric flow in the upper symmetric regime is stable due to stratification.

Though geometry of Cz configuration is different from the rotating annulus experiments, similarity of the flow field structure in between has been paid much attention [16, 17]. Compared to moderate and high Pr-number fluids, studies on hydrodynamic stability of low Pr-number Cz-melts (Si, GaAs, InP), initiated by Ristorcelli and Lumley [16] and Kakimoto [17], appears to be scare. This is more pronounced in the case of GaAs melt for which the convective flow was studied by Polezahaev et al [18]. Using an axisymmetric modeling of fluid flow without a swirl, the critical Grashof number was estimated to be as high as ~ for GaAs/Cz system of the aspect ratio [18]. They have shown that the critical number for the onset of thermal oscillations in the melt decreases to ~ when the melt depth increased, namely for . However, it is well-known [19] that for a low Pr melt rotating with its container, the critical Rayleigh number increases with the rotation rate. The so-called overstability associated with rotation intensity, namely the Taylor number, is an important feature of convection with rotation [20].

The main purpose of the present work is to investigate the flow field structure of the GaAs/Cz melt. The effect of rotationally driven- and thermocapillary forces on the flow pattern is studied. Both rotating Rayleigh-Bénard instability [21, 22] and the baroclinic instability [17, 23] are to be considered. The mathematical model developed in the present study incorporates transport processes of all domains of the system. The crystal is considered to be passive here and serves the purpose of enforcing an isothermal boundary condition at the crystallization front.

II. MODEL DESCRIPTION AND NUMERICAL SCHEME

2.1. Physical Model and Basic Assumptions

The idealized geometry of a modified Cz puller, the computational domains and the coordinate system adopted in the present analysis are illustrated in figure 1. The system is assumed to be in a pseudo-steady state and the axi-symmetric. Continuity, Navier-Stokes and energy equations are solved with the Boussinesq approximation. Both the GaAs melt and the encapsulant are incompressible Newtonian fluids with laminar flows. Thermophysical properties of the system are constant except for the temperature-dependency of the encapsulant dynamic viscosity, μ_e. The crucible bottom is thermally insulated and its side wall of height (h_m+h_e) is at a uniform and constant temperature, T_c. The physical properties of the system used for simulations are given in reference [24]. The thermophysical properties of ambient gas (Argon) are summarized in Table 1. The geometrical as well as the process parameters used in the present simulations are given in Table 2.

Table 1: Physical properties of Gas used for simulations

Density, ρ_g	486.8295/T kg/m^3
Thermal conductivity, λ_g	0.01+(2.5×10^{-5}) ×T W/m.K
Specific heat, c_{Pg}	521 J/kg.K
Dynamic Viscosity, μ_g	8.466×10^{-6} + 5.365×10^{-8} T- 8.682×10^{-12} T^2

Table 2: Geometrical and process parameters used for simulation

Crucible radius, r_c	0.075 m
Crystal radius r_s	0.0375 m
Melt height, h_m	0.05 m
Encapsulant height, h_e	0.02 m
Insulating enclosure height, h_E	0.2 m
Characteristic length	L=[h^4_m/(r$_c$-r$_s$)]$^{1/3}$
Crystal height, h_s	0.12 m
Crystal rotational rate, Ω_x	5 rpm
Crucible rotational rate, -Ω_c	5-20 rpm
Pulling rate, u_p	10 mm/h
Crucible wall temperature, T_c	1529 K
Enclosure top temperature, T_a	1261 K
Insulating enclosure emissivity, ε_E	0.8

In this configuration, the counter rotation of the crystal $(r_s;\Omega_x)$ and crucible $(r_c;-\Omega_c)$ influences the flow field in the melt. In the present study, a set of numerical simulations was performed for a 37.5mm radius crystal, 75mm radius crucible and 50mm height melt. Hence, the ratio between the Reynolds numbers Re_c and Re_s equals to $4\left|\Omega_c/\Omega_x\right|$ by definition of $\mathrm{Re} = r^2\Omega/\nu$. Throughout the calculations, Ω_x is assumed to be constant and equal to a reasonably [25] small value $(5\ rpm \cong 0.524\ rad/s)$ while the crucible rotation rate varies from -5 to -20 rpm.

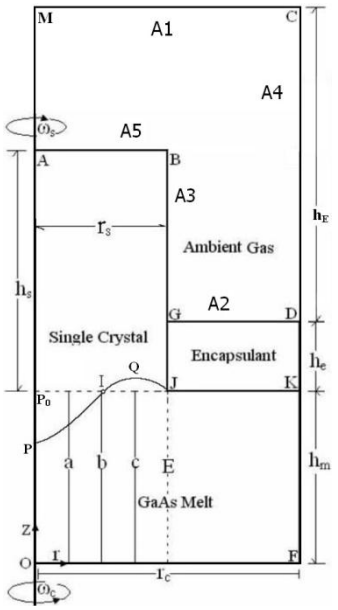

Figure 1: Sketch of a modified Czochralski crystal growth setup and the computational domains. The curve PIJ represents the M-type experimental interface shape on which the point I is the inflection point.

2.2. Mathematical Model

Throughout the present simulations, the Reynolds number of the GaAs melt flow field $\mathrm{Re}_m = u_{\max} L / \nu$, does not exceed the computationally obtained [25] Re_x^* and/or Re_c^* values. This may ensure the validity of the axisymmetric flow assumption in the present modeling. Therefore, all variables $\Phi = \Phi(r, z)$ in Table 3 are independent of the azimuthal θ angle and the numerical model solves three momentum equations for three velocity components, u_r, u_z and u_θ in two-dimensional space. The variations in the fluid density are ignored except insofar as their effect on the gravitational force.

Table 3: The diffusion coefficient Γ_Φ and source term S_Φ for variable Φ

Φ	Γ_Φ	S_Φ
1	0	0
u_z	μ	$-(\partial p/\partial z) + \rho g \beta (T - T_{ref})$
u_r	μ	$-(\partial p/\partial r) - \mu u_r / r^2 + \rho u_\theta^2 / r$
u_θ	μ	$-\mu u_\theta / r^2 - \rho u_r u_\theta / r$

Based on these assumptions, the generalized transport equation (GTE), governing the fluid flow and heat transfer in this arrangement, can be expressed in polar-cylindrical coordinate system as

$$\frac{\partial}{\partial z}(\rho u_z \Phi) + \frac{1}{r}\frac{\partial}{\partial r}(\rho r u_r \Phi) = \frac{\partial}{\partial z}\left(\Gamma_\Phi \frac{\partial \Phi}{\partial z}\right) + \frac{1}{r}\left(r\Gamma_\Phi \frac{\partial \Phi}{\partial r}\right) + S_\Phi \ , \qquad (1)$$

for which the diffusion coefficient Γ_Φ and the source term S_Φ for dependent variables Φ are listed in Table 3. The first and the last rows in Table 3 are the expressions of continuity and the energy equations, respectively. The energy loss due to viscous dissipation is neglected. T_{ref} is the reference temperature for the Boussinesq approximation, p the reference pressure, β the coefficient of volumetric expansion and g is the gravitational acceleration constant.

In the present cylindrical model, the streamline function ψ and vorticity ω are defined in terms of the radial and axial velocities as $u_r = -(1/r)(\partial\psi/\partial z)$, $u_z = (1/r)(\partial\psi/\partial r)$ and $\omega = \partial u_r/\partial z - \partial u_z/\partial r$. Physically ψ is a measure of the volume flux. So the difference between the values of ψ at two points in the meridional plane is proportional to the meridional flux between them. The vorticity is associated with rotational motion and in a 2D flow the vorticity vector is orthogonal to the plane of flow.

2.3. Boundary conditions

Corresponding to the boundaries defined in figure 1, the conditions applied to the system are listed in Table 4. Altogether, three types of flow boundary conditions were used for the whole set of computations: no slip boundary for the crucible, crystal and insulator, no shear stress on symmetry axis and Marangoni boundary condition for both the encapsulant free surface and the melt/encapsulant interface. The numerically approximated temperature [24] at the crucible side wall ($0 < z < (h_m + h_e)$) was employed as a constant. Corresponding to the heat input around 1.5 kW in the case of mixed convection, T_c=1529 K is suitable for growth of 3″ diameter GaAs crystal providing the pull rate ~ 10-15 mm/h in the growth process. The crucible bottom is insulated and assumed to be adiabatic. Above the crucible top end, the temperature of the insulating enclosure wall, T_E is assumed to be variant as given in Table 4. The top enclosing wall is at the same temperature as the ambient T_a=1261 K. Both the temperatures along the crucible bottom and the enclosure top surface are of considerable importance for the control of the GaAs/Cz process, particularly for the shape of CMI.

Table 4: The applied boundary conditions corresponding to Figure 1.

	u_z	u_r	u_θ	T
OP_0	$\frac{\partial u_z}{\partial r} = 0$	0	0	$\frac{\partial T}{\partial r} = 0$
AP_0	u_P	0	0	$\frac{\partial T}{\partial r} = 0$
AB	0	0	$r\,\Omega_x$	$-\lambda_s \frac{\partial T_s}{\partial z} = h_{sg}(T_s - T_a) + \varepsilon_s \sigma (T_s^4 - T_{eff}^4)$
AM	0	0	0	$\frac{\partial T}{\partial r} = 0$
MC	0	0	0	T_a
DC	0	0	0	$T_z = (T_C - T_a)\left[\frac{h_E - h_z}{h_E}\right]^6 + T_a$
KD	0	0	$r_C \Omega_C$	T_c
FK	0	0	$r_C \Omega_C$	T_c
OF	0	0	$r\,\Omega_C$	$\frac{\partial T}{\partial z} = 0$
JK	0	$\mu_m \frac{\partial u_r}{\partial z} = \frac{\partial \gamma_m}{\partial T}\frac{\partial T_m}{\partial r}$	$\frac{\partial u_\theta}{\partial z} = 0$	$-\lambda_m \frac{\partial T_m}{\partial z} + \lambda_e \frac{\partial T_e}{\partial z} = \alpha_e \varepsilon_m \sigma (T_m^4 - T_{eff}^4)$
JG	u_P	0	$r_x \Omega_x$	$-\lambda_s \frac{\partial T_s}{\partial r} + \lambda_e \frac{\partial T_e}{\partial r} = \alpha_e \varepsilon_s \sigma (T_s^4 - T_{eff}^4)$
GB	u_P	0	$r_x \Omega_x$	$-\lambda_s \frac{\partial T_s}{\partial r} = h_{sg}(T_s - T_a) + \varepsilon_s \sigma (T_s^4 - T_{eff}^4)$
GD	0	$\mu_e \frac{\partial u_r}{\partial z} = \frac{\partial \gamma_e}{\partial T}\frac{\partial T_e}{\partial r}$	$\frac{\partial u_\theta}{\partial z} = 0$	$-\lambda_e \frac{\partial T_e}{\partial z} = h_{eg}(T_e - T_a) + \varepsilon_e \sigma (T_e^4 - T_{eff}^4)$

The effective temperature, $T_{eff,\,k}$ which appears in Table 4, is due to radiative heat exchange in the present system. According to the Gebhart theory of radiation, the net radiative heat exchange between an exposed surface k at temperature T_k, and all others in an N-sided enclosure can be calculated as:

$$q_k = \varepsilon_k \sigma T_k^4 - \frac{1}{A_k}\sum_{i=1}^{N} G_{ik}\,\varepsilon_i \sigma T_i^4 A_i = \varepsilon_k \sigma (T_k^4 - T_{eff,k}^4) \qquad (2)$$

Where A_k is the area of the surface k and

$$T_{eff,k} = \left(\frac{1}{A_k \varepsilon_k}\sum_{i=1}^{N} A_i \varepsilon_i G_{ik} T_i^4\right)^{1/4} \qquad (3)$$

is the effective temperature to which the surface k loses heat by radiation. The Gebhart factor,

$$G_{ik} = F_{ik}\varepsilon_k + \sum_{j=1}^{N} F_{ij}(1-\varepsilon_j) G_{jk} \qquad (4)$$

represents the fraction of out-going flux from surface i that absorbed by surface k. The calculation procedure for the view factor matrix F(i,j) is straightforward for meniscus free surface. The above set of linear equations for G_{ik} (i, k =1,2,…,N) can be solved by Gaussian elimination. Repeating the calculations for all surfaces by changing k, one obtains all the Gebhart factors. For N=5 flat-zones enclosure in the present configuration, the number of independent view factors to be determined is only (N/2)(N-3)=5.

2.4. Numerical model

The two-dimensional differential equations (1) with the boundary conditions for the fluid flow and heat transport in the Cz configuration were solved numerically by the finite volume method (FVM). The computational domain was discretized into a finite number of control volumes over which the governing equations were integrated. The resulting system of algebraic equations was solved iteratively until convergence was reached. A staggered grid system was employed for different dependent variables. The pressure p, the azimuthal velocity u_θ, and the temperature T were calculated at the grid point in the center of the main control volume (MCV); the axial and radial components of velocity u_z and u_r, respectively, were staggered in the z and r directions to the mid-point of the boundaries of MCV. The SIMPLEC algorithm [26] was used to couple velocities and pressure on staggered grids. The grid used in the present calculation is uniform for the computational domain of melt, encapsulant, crystal and the ambient gas. It contains 52×272 grid points with spacing of $1.0\,mm$ resulting in a grid-independent solution. For all variables Φ, the solution was deemed convergent when the criterion $\left|\Phi^{n+1} - \Phi^{n}\right|_{\max} \le 10^{-4}$ was satisfied where n represents the index of iteration number. The accuracy of the numerical code was ascertained by validating the general results of the present calculation with the experimental [11, 27] and 2D numerical [6, 9] results obtained for corresponding geometry and boundary conditions. Remarkable is the particular shape of CMI which appears in the present simulations as obtained in the model analyses of both liquid encapsulated Czochralski and VCz growth of GaAs bulk crystals.

III. RESULTS AND DISCUSSION

In this section, the nature of the GaAs/Cz melt convective flow is described. The results obtained from the numerical simulations are presented. The influence of rotationally-driven forces on the flow field structure and temperature distribution is discussed.

3.1. Description of the flow field structure

The convection instabilities in Czochralski melt are among the most challenging issues in bulk crystal growth modeling. This is mainly due to the complexity of hydrodynamics and associated heat transport in the melt from which a crystal is growing. In the present model, the flow instability can exhibit unique features because of coexisting vertical nad horizontal temperature gradients and the differential rotation rates of the crystal ($r_x ; \Omega_x$) and crucible ($r_c ; -\Omega_c$). The minus sign here means the counter-clockwise direction of rotation. For a liquid rotating with its container, besides the gravity, it is necessary to include two body forces, the centrifugal force representing a vector derivative $\boldsymbol{\Omega}_c \wedge (\boldsymbol{\Omega}_c \wedge \mathbf{r})$ and the Coriolis force $2(\boldsymbol{\Omega}_c \wedge \mathbf{u})$ with $\mathbf{r}$ and $\mathbf{u}$ as the position and velocity vectors, respectively. The effects of centrifugal force are usually neglected in model calculations, particularly for the crystal growth set-ups, and the analysis has largely been restricted to consideration of the interaction between the Coriolis and buoyancy forces. In the GaAs melt, the natural convection may readily become unsteady and time-dependent because of its low Pr number. Even with small driving temperature differences, $\Delta T_{\max} = 18\,K$ imposed on the system ($h_m / r_c = 0.67$), the Grashof number Gr_m was found to be of order 10^7. However, compared to its critical number calculated for 2D melt without a swirl [18], the flow may be assumed to be axisymmetric in the present model in which the melt is rotating with its container.

The crystal rotation generates an upward flow in the melt central column which encounters the large-scale circulation (LSC) caused by the crucible rotation in the same direction as the buoyancy and thermocapillary convections. In the configuration with $\mu < 0$ as the rotation ratio $-\Omega_c / \Omega_x$ and the radius ratio of $\eta = r_x / r_c = 0.5$, this can be readily verified that $\mathrm{Re}_c / \mathrm{Re}_x = 4\mu$. With a constant and reasonably small [25] $\Omega_x = 0.524\ rad/s$ throughout the calculations, the large-scale flow was found to be the dominant feature of the flow pattern. The parameter $\mathrm{Ra}/\mathrm{Pr}.\mathrm{Re}_c^2$ is so high (~10), compared to $\mathrm{Ra}/\mathrm{Pr}.\mathrm{Re}_x^2$ that the upward central flow does not appear in the present simulations. In fact, only for $\Omega_c \le 0.417\ rad/s$ (~4.0 rpm), the governing parameter $(\mathrm{Ra}/\mathrm{Pr}.\mathrm{Re}_c^2) \ge 1$ can be held. Hence, the reason for an eventual instability in the system is coupling of thermal convection and the forces generated by the crucible rotation. Furthermore, the surface tension to buoyancy ratio $\mathrm{Ma}/\mathrm{Pr}.\mathrm{Gr}^{1/2}$ for the GaAs melt is large enough (~180 compared to ~120 in[16] for Si) to modify the structure of the flow. However, as illustrated in figure 2, the effect is strongly controlled by the presence of highly viscous ($\mu_e / \mu_m \sim 10^3$) encapsulated layer on the GaAs melt surface. Far from the melt/encapsulant boundary, the flow velocity vectors and temperature profiles in the melt are influenced by

thermocapillary forces. This effect leads to a more convex to melt interface by changing slightly the direction of the velocity vectors in peripheral part of the phase boundary. The flow velocity vectors close to the melt/encapsulant interface were found to be so small (see figure 2) and the flow remained in a steady state as assumed in the present model. This can be inferred that, for the GaAs melt/encapsulant system, the effective critical Ma number should be far beyond the estimated $\sim 6.9 \times 10^{4} (\mathrm{Pr})^{1.36}$ value [28] for low Pr melts.

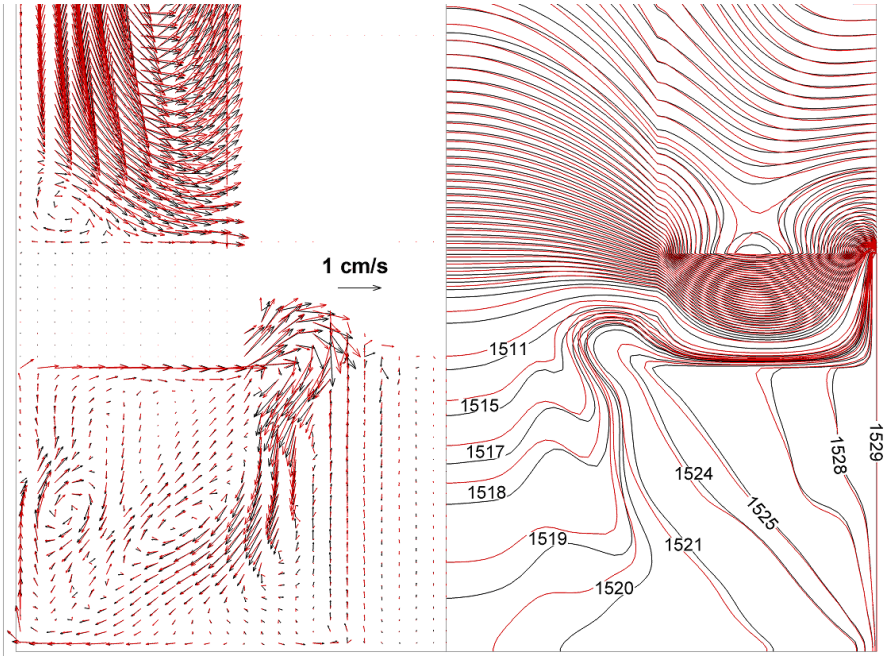

Figure 2: Marangoni effect (black lines) on the velocity field (left) and temperature distribution (right). The rotation rates for crystal and crucible are +5 and -5 rpm, respectively.

For the GaAs melt in a rotating Cz crucible, the Coriolis force largely influences the buoyancy-driven flow due to coupling of the radial velocity with the fluid rotation. Though the Coriolis force stabilizes the fluid flow due to the prevention of vertical convection, it complicates however the structure of the flow field by increasing the curvature the fluid particle-paths. Therefore, hydrodynamics of the GaAs melt in a non-inertial frame is characterized by the Taylor number T_a and thermal Rossby number Ro_T. By definition Ta stands for the ratio of Coriolis force to the viscous force, and the Rossby number is the ratio between convective acceleration and the Coriolis force. Non-dimensional parameters related to the present model are given in Table 5.

Table 5. Dimensionless similarity parameters for the GaAs melt convection with the rotation. The characteristic length $L = 5.503 \times 10^{-2}\ m$, $\Delta T_{\max} = 18\ K$, $\Omega_x = 0.524\ rad/s$ and $\Omega_x \le \Omega_c \le 2.094\ rad/s$.

$\mathrm{Ra} = (g\beta/\nu\alpha) L^3 \Delta T_{\max}$	1.574×10^{6}
$\mathrm{Ma} = (\gamma_T/\mu\alpha) L \Delta T_{\max}$	5.928×10^{4}
$\mathrm{Re}_x = r_x^2 \Omega_x / \nu$	1.511×10^{3}
$\mathrm{Re}_c = r_c^2 \Omega_c / \nu$	$1.153 \times 10^{4} \Omega_c$
$\mathrm{Ta} = 4\Omega_c^2 (r_c - r_x)^5 / \nu^2 L^2$	$2.744 \times 10^{7} \Omega_c^2$
$\mathrm{Ro}_T = g\beta \Delta T_{\max} L / \Omega_c^2 (r_c - r_x)^2$	$1.292 / \Omega_c^2$

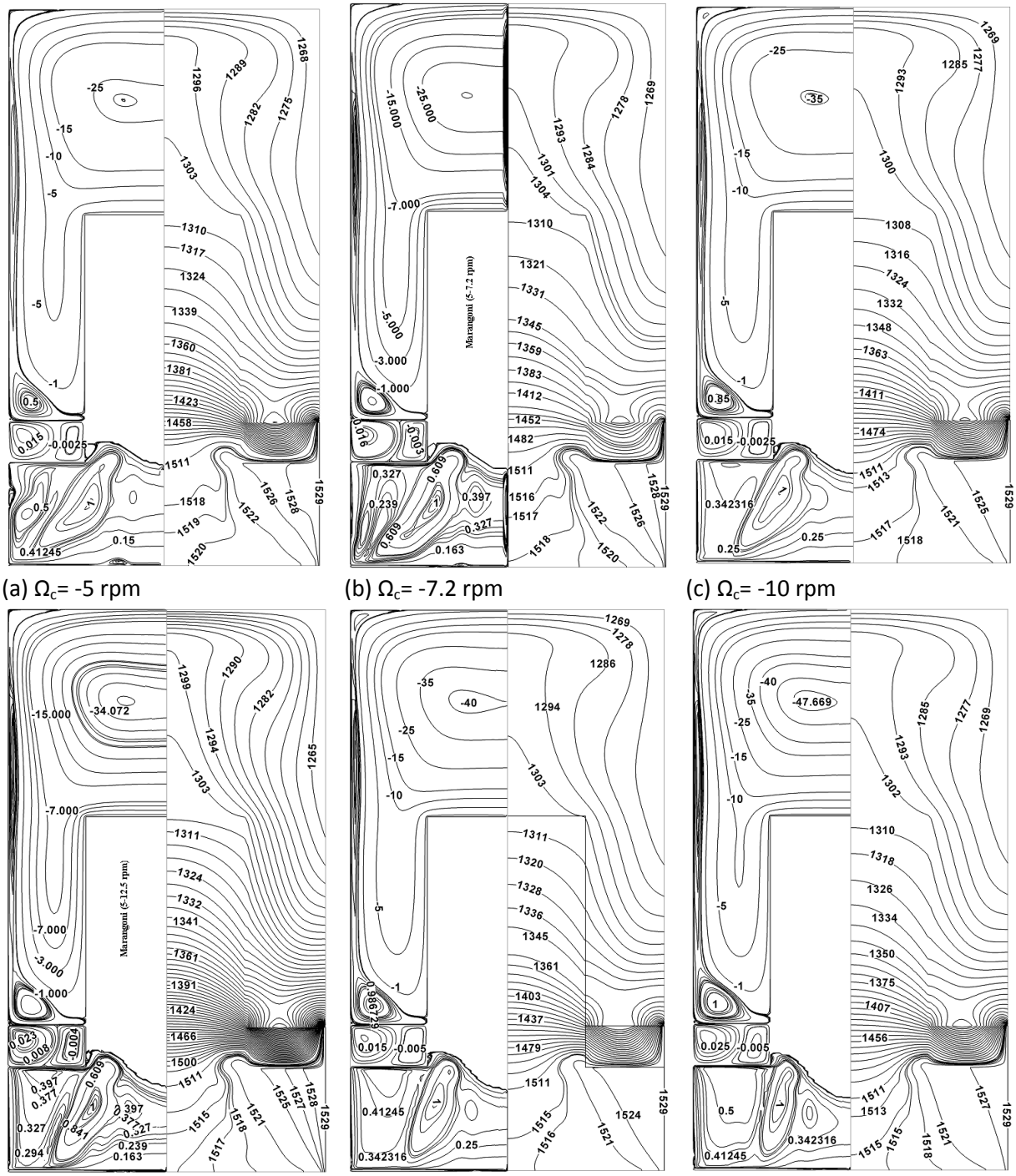

(a) Ω_c= -5 rpm (b) Ω_c= -7.2 rpm (c) Ω_c= -10 rpm

(d) Ω_c= -12.5 rpm (e) Ω_c= -15 rpm (f) Ω_c= -20 rpm

Figure 3 (a-g): Contours of stream function (left) and temperature (right) with $\mathrm{Ra} = 1.574 \times 10^{6}$, $\mathrm{Ma} = 5.928 \times 10^{4}$, $\mathrm{Re}_x = 1.511 \times 10^{3}$ for different crucible rotation rates.

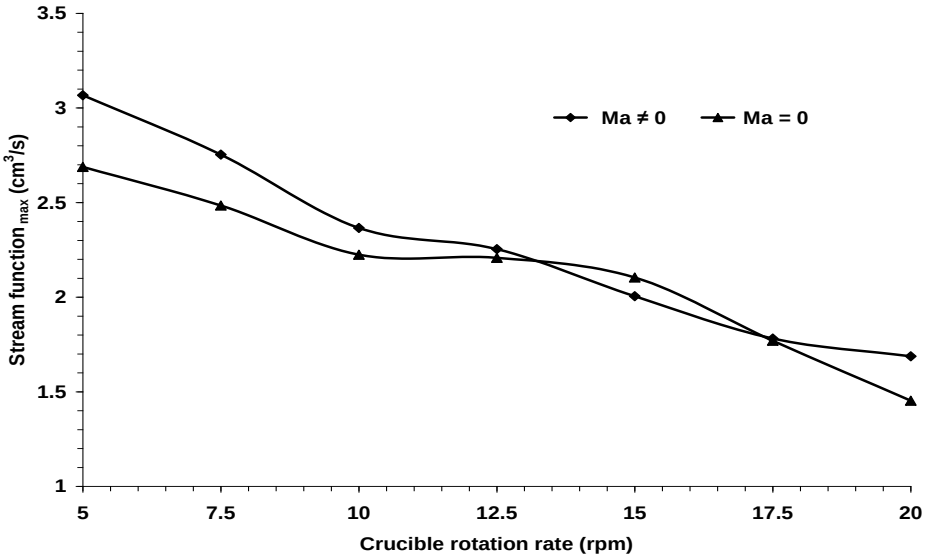

Figure 4: Maximum intensity of the convection as a function of the rotation rate.

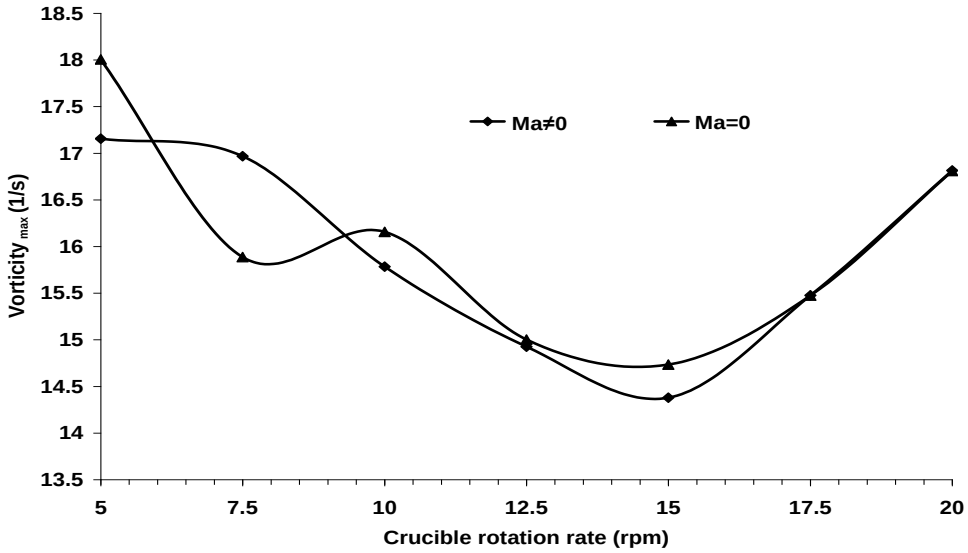

Figure 5: Maximum vorticity of the flow as a function of the rotation rate.

3.2. Simulation of the flow field and temperature distribution

In the GaAs melt rotating with its container, the flow field and heat transport are influenced by the impact of Coriolis force on the thermal convection flow. The flow field and temperature distribution are illustrated in figure 3 (a-g) for the melt characterized by $\mathrm{Ra}_m = 1.574 \times 10^6$, $\mathrm{Ma} = 5.928 \times 10^4$, $\mathrm{Re}_x = 1.511 \times 10^3$. The crucible rotation varies in the range $0.524 \le |\Omega_c| \le 2.094\ rad/s$. To describe the multi-cell structure of the flow, the line b ($r = r_x/2$, $z = h_m$), crossing approximately the inflection point (I) on the phase boundary, and the line E as the edge of the melt central column (see figure 1) are used.

As for any rotating stratified fluid in a container [20] the structure of the flow is dominated by a centrifugally-driven large-scale circulation (LSC). The roll (LSC) is characterized by $\psi(r,z)/\psi_{\max} = 1$ and found to be headed towards the peripheral concave to melt part of the phase interface. For all cases, the central position of LSC lies approximately on the edge E nearby the point M_i ($r = r_c/2$, $z = h_m/2$) in the interior of the melt. As shown in figure 3 (a-g), at lower rotation rates $|\Omega_c| \le \Omega_x$ the dominant cell is tailed to the corner and compressing the buoyancy driven flow near the wall makes a tilt angle θ_ψ with respect to the vertical line E.

Increasing $|\Omega_c|$, the LSC rotates around the vortex vector $\boldsymbol{\omega}_{\max}$ so that θ_ψ decreased and the buoyancy driven convection is expanded and the flow pattern between the wall and the edge, E is considerably simplified.
Figure 4 shows that the intensity of the convection, $\psi_{\max}$ strongly depends on the rotation rate. Coupling to the radial velocity of the flow, the Coriolis force enhancement has a restrictive effect on the centrifugally forces, pronounced more at the lowest and the highest rotation rates (see figure 4), does not change the trend. Associated to the centrifugally driven flow, the vortex $\omega_{\max} = (1/r)\{\partial^2\psi/\partial r^2 + \partial^2\psi/\partial z^2 - (1/r)\partial\psi/\partial r\}$ magnitude is affected by the Coriolis and thermocapillary forces.
The numerical results, with and without Marangoni flow, are plotted in figure 5. Increasing the rotation rate, $\omega_{\max}$ is lowered to a minimum at around $|\Omega_c| = 1.571\ rad/s$ (~15 rpm), and the raised sharply by further increase in Ω_c. Again, thermocapillary forces modify the curve, particularly in the lower range of rotation, but the general feature of the curve remains the same. For the GaAs melt parameterized in the model by so high $\mathrm{Ma}/\mathrm{Pr}\,\mathrm{Gr}^{1/2}$ as ~180, the result is unexpected.

According to the scaling analysis, in the interior of the melt $\psi_\sigma/\psi_\beta = 4(\mathrm{Ma}/\mathrm{Pr})^{1/3}/\xi^{1/2}Gr^{1/2}$, where ψ_σ and ψ_β are the magnitudes of Marangoni and buoyancy flow stream functions, respectively and ξ appears in $\Delta T_M = \xi\,\Delta T_{\max}$ [29]. The temperature at the point M_i was computed for the applied range of rotation and found to be $T_M = 9.5 \pm 1.4\ K$ leading to $\xi \sim 0.53$ and $\psi_\sigma/\psi_\beta \sim 1/10$.

It was found that the tilt angle, θ_ψ is directly related to the Ekman shear angle in its model-adopted form $\chi(r) = 4.746 \times 10^{-3}\pi^2\Omega_c(r_c^2 - r^2)$, simply by $\tan\theta_\psi = 1 - \tan\chi(r)$ at the point K ($r = r_c/2$, $z = \delta_E$) on the line E close to the crucible bottom. Herein, the angles are in degrees, Ω_c in rpm, $r_c = 7.50\ cm$, and $\delta_E = (\nu/|\Omega_c|)^{1/2}$ is ~1.0 mm for $\Omega_c = -5.0\ rpm$ as the Ekamn layer thickness. Increasing in Ω_c, the number of spiral arms $N_E = |\mathrm{Re}_c|/16\pi$ with separation $\Delta r = (1/4N_E)(r_c^2/r)$, increases. This can be readily verified that the line E separates apart the smaller spirals near the corner and the larger spirals near the axis of rotation, corresponding to the smaller and larger deformations of the flow volume element. Supposed that increasing the rotation rate intensifies the effect and referred to the simple relation between θ_ψ and $\chi(r)$, development of the spiral shearing flow might be assumed to explain the LSC rotation around the vortex vector $\boldsymbol{\omega}_{\max}$.

3.3. Flow modes in the GaAs melt rotating with its container

Referred to figure 3 (a-g)**,** it appears that between the LSC and the rotation axis, there is an ovidal shape small roll with $\psi/\psi_{\max} \sim 0.4$**.** The cell is located below the convex to melt part of the phase boundary and centered approximately on the line b crossing the inflection point I on the crystallization front. Emerged from the centrifugally driven cell, and circulating in the same direction as LSC, the intensity of this small convection found to be, in contrast to LSC, approximately independent of the rotation rate. Its shape, however, is modified by increasing Ω_c. for lower rotation rates, $|\Omega_c| < 7.5\ rpm$ and at the same shape, the thermal field exhibits an undulating structure in the melt leading to a radial non-uniformity of the thermal field close to the phase boundary. The effect is suppressed by further increase in the rotation rate ($|\Omega_c| > 7.5\ rpm$) due to the overstability known [20] as a distinctive feature of convection with rotation. This behavior implies that the Rayleigh-Benrad instability occurs at low rotation rates. In fact, when the buoyancy and Coriolis forces are comparable, $(\mathrm{Gr/Ta}) \sim 1$, the Coriolis force will prevent vertical convection against the conservation of angular momentum and the oscillations decrease close to the onset boundaries. Herein, the ratio $\mathrm{Gr/Ta}$ equals to unity when $|\Omega_c| = 8.78\ rpm$ as confirmed by simulations of the fields in figure 3(a-f).

For the imposed and calculated (at the point M_i) temperature differences $\Delta T_r = \Delta T_{\max}$ and $0.8 \le \Delta T_{m,i} \le 12.5\ K$, respectively, the flow modes in the GaAs melt rotating at different rates are represented in figure 6 as the two-parameter regime diagram. Note that $\partial T/\partial z \cong 4.2\ K/cm$ at the point M_i found to be close to the data given by Kaoi et al [30]. Therefore, the vertical temperature difference ΔT_z is close to $\Delta T_{m,i}$ in the model.

The knee-shaped curve of transition obtained from the experimental results [15] for mercury ($\mathrm{Pr} = 2.46 \times 10^{-2}$) shows that, at lower rotation rates the flow appears to be axisymmetric in the regime diagram. As mentioned before, the flow field is dominated by the Küppers-Lortz instability for $|\Omega_c| < 8.77\ rpm$. The enhancement of Coriolis forces complicates the flow pattern due to the baroclinic instability. Numerical results in figures 7(a) and 7(b) reveal that how the local temperature difference and velocity components at the mid-depth/mid-radius of the melt, namely at the point M_i in the interior, vary with rotation. For more realistic case in the model, that is when $\mathrm{Ma} \neq 0$, both $u_{m,i}$ and $T_{m,i}$ decrease considerably with Ω_c in the lower range of rotation $5 < |\Omega_c| < 10\ rpm$. Remarkably, the flow velocity $u_{m,i}$ is raised by a further increase in Ω_c up to a maximum at $\Omega_c = -12.5\ rpm$ and then lowered more sharply in higher range of rotation, $12.5 < |\Omega_c| < 15.0\ rpm$. Decreasing $T_{m,i}$ in the lower rotation range corresponds to higher value of the Rossby number Ro_T (due to larger $\Delta T_{m,i} = T_c - T_{m,i}$) and lower values of the Taylor number ($\mathrm{Ta} < 10^7$) in the regime diagram. By further increase in Ω_c , the onset of a baroclinic wave occurs at $\mathrm{Ro}_T = 2.06$ ($\Delta T = 18\ K$ and $\Omega_c = -7.2\ rpm$) corresponding to $\mathbf{Ta} = 1.417 \times 10^7$. For silicon melt, this critical Rossby number was 2.4 according to theoretical investigations [31]. The points which lie on the line II (see figure 6) stand for non-axisymmetric flow with regular wave [15]. At rotation rates $|\Omega_c| \geq 15\ rpm$ and for the imposed $\Delta T = \Delta T_{\max}$, the points located under the line II represent the stabilization of the flow at $\mathrm{Ro}_T \leq 0.476$ and $\mathrm{Ta} \geq 6.152 \times 10^7$. The transition is qualitatively similar to experimental data [32] in which it occurs at Ro_T number considerably lower than unity.

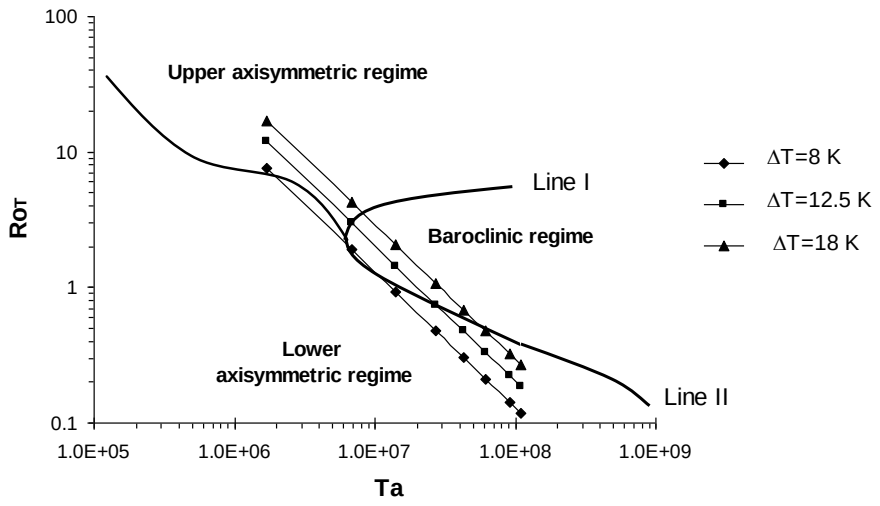

Figure 6: Flow modes at different rotation rates ($2.5 \leq \Omega_c \leq 20\ rpm$) for the imposed horizontal and vertical temperature differences $\Delta T_r = 18\ K$ and $8.0 \leq \Delta T_z \leq 12.5\ K$, respectively. The transition curve obtained from Fein-Pfeffer's experimental results [15]. The two lines stand for the upper and the lower boundaries for the occurrence of baroclinic instability.

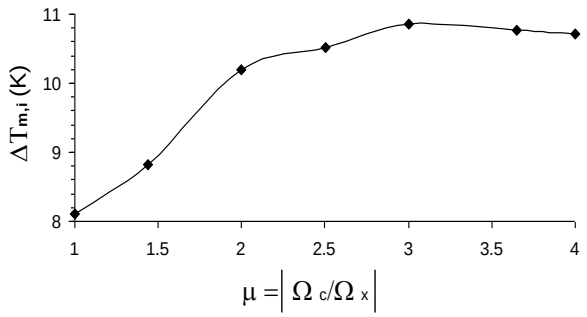

Figure 7(a): Rotational effect on temperature variation in the interior of the melt.

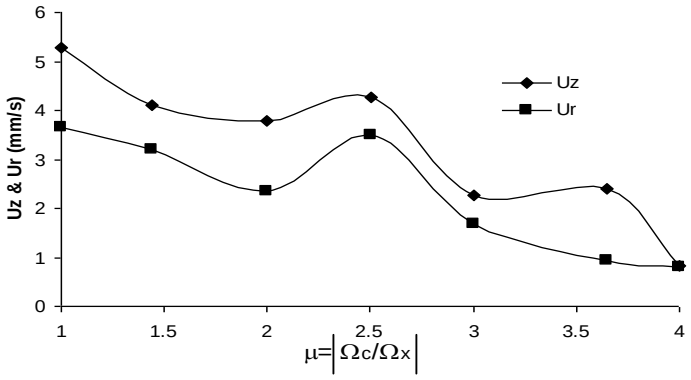

Figure 7(b): Rotational effect on the components of flow maximum velocity in the interior of the melt.

IV. CONCLUSION

The GaAs flow field structure and temperature distribution were described in the present model calculations. It was demonstrated that even perfectly axisymmetric geometries may exhibit flow instabilities. Simulations of the melt flow even at the lowest applied rotation rate $\Omega_c = -0.524\ rad/s$ revealed that buoyancy driven flow characterized by a unicellular meridional circulation is compressed by a strong centrifugally driven roll (LSC). Throughout the simulations, LSC appeared as the dominant flow in the multicell structure of the GaAs melt rotating with its container. In contrast to the large magnitude of $Ma/Pr\,Gr^{1/2}$, it was shown that the convective flow pattern does not depend strongly on the presence of thermocapillary forces. In fact, in the interior of the melt ψ_β/ψ_σ as the ratio between the buoyancy and thermocapillary forces largely exceeds the unity.

Increasing the rotation rate $0.524 < |\Omega_c| < 2.094\ rad/s$, the dominant cell (LSC) found to rotate around the vortex vector $\boldsymbol{\omega}_{\max}$ by an angle θ_ψ directly related to the Ekman shear angle. Decreasing the intensity of the cell, the Coriolis force enhancement suppresses the undulating structure of thermal field. The so-called overstability of the melt was broken by further in the rotation rate. The appearance of the baroclinic wave region in the flow regime diagram corresponds to the transition from axisymmeteric to non-axisymmetric flow. The transition found to be sensitive to the applied temperature difference and as ΔT increases, a regular wave gives way to an irregular wave. The onset of baroclinic wave found to occur at $Ro_T = 2.07$ when $\Delta T = 18\ K$. According to the experimental analysis [32] the transition is associated with significant increase in the amplitude of temperature fluctuation close to the phase boundary. As shown in the regime diagram, the baroclinic thermal wave disappears when the rotation-driven convection overcomes the buoyancy-driven convection.

The present model analysis may ensure axisymmetric flow and thermal fields in the melt characterized by $Ro_T \le 0.476$ and $Ta \ge 6.152 \times 10^7$. The results correspond to the rotation rate $|\Omega_c| \ge 1.571\ rad/s$ and $\mu = |\Omega_c/\Omega_x| \ge 3$, close to the parameters used in the industrial scale growth ($|\Omega_c| = 1.676\ rad/s$ and $\mu = 2.7$) of the GaAs crystals. Notable is that the vortex of the dominant circulation $\boldsymbol{\omega}_{\max}$ found to meet its minimum value at around $|\Omega_c| = 1.571\ rad/s$.

REFERENCES

[1.] M.R. Brozel, I.R. Grant, Growth of gallium arsenide, in: P. Capper (Ed.), Bulk Crystal Growth of Electronic, Optical and Opto-electronic Materials, John Wiley, UK, 2005, pp. 43-71.
[2.] J.B. Mullin, Progress in the melt growth of III-V compounds, J. Cryst. Growth 264 (2004) 578-592.
[3.] A. Yeckel, J. J. Derby, Computational simulations of the growth of crystals from the liquid, in: H.J. Scheel, T. Fukada (Eds.), Crystal Growth Technology, John Wiley, UK, 2003, pp.115-137.
[4.] V.I. Polezhaev, Modelling of hydrodynamics, heat and mass transfer processes on the basis of unsteady Navier-Stokes equations. Applications to the material sciences at earth and under microgravity, Comput. Methods Appl. Mech. Engrg. 115 (1994) 79-92.
[5.] T. Tsukada, M. Kobayashi, C.J. Jing, N. Imaishi, Numerical simulation of Cz crystal growth of oxides, FDMP 1 (2005) 45-62.
[6.] S. Gondet, T. Duffar, G. Jacob, N. Van der Bogart, F. Louchet, Thermal stress simulation and interface destabilisation in indium phosphide grown by LEC process, J. Cryst. Growth, 198/199 (1999) 129-134.
[7.] N. Miyazaki, H. Kutsukake, A. Kumamoto, Development of 3D dislocation density analysis code for annealing process of single crystal ingot, J. Cryst. Growth 243 (2002) 47-54.
[8.] M. Jurisch, St. Eichler, The development of LEC technology for GaAs single crystal growth from laboratory scale to mass production, in: Proceeding of the Czochralski Symposium, Torun/Kcynia, Poland, 2003.

[9.] D. Vizman, S. Eichler, J. Friedrich, G. Muller, Three-dimensional modeling of melt flow and interface shape in the industrial liquid-encapsulated Czochralski growth of GaAs, J. Cryst. Growth 266 (2004) 396-403.
[10.] K. Koai, Model-based thermal stress control of LEC GaAs bulk crystal growth, PhD thesis, Mechanical Engineering Department, MIT, Cambridge, MA (1990).
[11.] M. Shibata, T. Suzuki, S. Kuma, T. Inanda, LEC Growth of Large GaAs Crystals, J. Cryst. Growth 128 (1993) 439-443.
[12.] T.C. Chen, H.C. Wu, C. I. Weng, The effect of interface shape on anisotropic thermal stress of bulk single crystal during Czochralski growth, J. Cryst. Growth 173 (1997) 367-379.
[13.] S. Chandrasekhar, Hydrodynamics and Hydromagnetic Stability, Clarenden Press, Oxford, 1961.
[14.] P.C. Drazin, w.H. Reid, Hydrodynamic Stability, Cambridge Univ. Press, Cambridge, 1981.
[15.] J.S. Fein, R.L. Pfeffer, An experimental study of the effects of Prandtl number on thermal convection in a rotating, differentially heated cylindrical annulus of fluid, J. Fluid Mech. 75 (1976) 81-112.
[16.] J.R. Ristorcelli, J.L. Lumely, Second order turbulence simulation of Cz crystal growth melt, J. Cryst. Growth 129 (1993) 249-265.
[17.] K. Kakimoto, Flow instability during crystal growth from the melt, Prog. Cryst. Growth and Charat. 30 (1995) 191-215.
[18.] V.I. Polezhaev, O.A. Bessonov, N.V. Nikitin, S.A. Nikitin, Convective interaction and instabilities in GaAs Czochralski model, J. Cryst. Growth 230 (2001) 40-47.
[19.] F. Rosenberger, Fundamental of crystal growth I, Springer, Berlin, 1979.
[20.] E.L. Koschmieder, Benard Cells and Taylor Vortices, Cambridge Univ. Press, Cambridge, 1993.
[21.] J.R. Ristorcelli, J.L. Lumely, Instabilities, transition and turbulence in the Czochralski crystal melt, J. Cryst. Growth 116 (1992) 447-460.
[22.] A. Rubio, J.M. Lopez, F. Marques, Onset of Küppers-Lortz-like dynamics in finite rotating thermal convection, J. Fluid Mech. 644 (2010) 337-357.
[23.] Th. von Larcher, C. Egbers, Experiments on transitions of baroclinic waves in a differentially heated annulus, Nonlinear Processes in Geophys. 12 (2005) 1033-1041.
[24.] M. Li, W. Hu, N. Chen, D. Zhang, Z. Tang, Numerical analysis of LEC growth of GaAs with an axial magnetic field, Int. J. Heat Mass Transfer 45 (2002) 2843-2851.
[25.] V.I. Polezhaev, Modeling of Technologically Important Hydrodynamics and Heat/Mass Transfer Processes During Crystal Growth, in: H.J. Scheel, T. Fukuda (Eds.), Cryst. Growth Technology, John Wiley & Sons, West Sussex, 2003, pp. 155-186.
[26.] J.H. Ferziger, M. Perić, Computational Methods for Fluid Dynamics, 3rd Edition, Springer, Berlin, 2002.
[27.] S. Carra, S. Fogliani, M. Masi, L. Zanotti, C. Mucchino, C. Paorici, Melt-solid interface shape in LEC GaAs crystals: comparison between calculated and experimentally observed shapes, J. Cryst. Growth 166 (1996) 641-645.
[28.] G. Müller, A. Ostrogorsky, Convection in melt growth, in: D.T.J. Hurle (Ed.), Handbook of Crystal Growth, Basic Techniques, Vol. 2b, North Holland, 1994, pp. 710-820.
[29.] A.D.W. Jones, Scaling analysis of the flow of a low-Pr number Cz melt, J. Cryst. Growth 88 (1988) 465-476.
[30.] K. Kaoi, A. Seidl, H.-J. Leister, G. Muller, A. Kohler, Modeling of thermal fluid flow in the liquid encapsulated Czochraslki process and comparison with the experiment, J. Cryst. Growth 137 (1994) 41-47.
[31.] Y. Kishida, M. Tanaka, H. Esaka, Appearance of a baroclinic wave in Czochralski silicon melt, J. Cryst. Growth 130 (1993) 75-84.
[32.] Y.S. Lee, C.H. Chun, Transition from regular to irregular thermal wave by coupling of natural convection with rotating flow in Czochralski crystal growth, J. Cryst. Growth 197 (1999) 297-306.

Figure and table captions *should be 10-point boldface Helvetica (or a similar sans-serif font). Callouts should be 9-point non-boldface Helvetica. Initially capitalize only the first word of each figure caption and table title. Figures and tables must be numbered separately. For example: "Figure 1. Database contexts" , "Table 1. Input data". Figure captions are to be centered below the figures. Table titles are to be centered above the tables.*